Case Study

Neuron

In Vivo Imaging of Human Sarcomere Twitch Dynamics in Individual Motor Units

Highlights

- A wearable microscope straps to the human body to study neuromuscular physiology
- The microscope reveals the contractile dynamics of single motor units
- Time courses of sarcomere displacements report muscle force generation dynamics
- Post-stroke spasticity patients exhibited abnormal involuntary sarcomere dynamics

Authors

Gabriel N. Sanchez, Supriyo Sinha, Holly Liske, Xuefeng Chen, Viet Nguyen, Scott L. Delp, Mark J. Schnitzer

Correspondence

delp@stanford.edu (S.L.D.), mschnitz@stanford.edu (M.J.S.)

In Brief

Sanchez et al. describe a wearable microscope that images the twitch dynamics of single motor units in the skeletal muscles of alert human subjects, revealing aspects of neuromuscular physiology never seen before in healthy subjects or those with movement disorders.

Sanchez et al., 2015, Neuron *88*, 1109–1120
December 16, 2015
http://dx.doi.org/10.1016/j.neuron.2015.11.022

CellPress

Neuron
Case Study

In Vivo Imaging of Human Sarcomere Twitch Dynamics in Individual Motor Units

Gabriel N. Sanchez,[1,4] Supriyo Sinha,[2,3] Holly Liske,[4] Xuefeng Chen,[4] Viet Nguyen,[5] Scott L. Delp,[1,4,*] and Mark J. Schnitzer[2,3,6,*]
[1]Department of Bioengineering
[2]Department of Biology
[3]Department of Applied Physics
[4]Department of Mechanical Engineering
[5]Department of Neurology
[6]Howard Hughes Medical Institute
Stanford University, Stanford, CA 94305, USA
*Correspondence: delp@stanford.edu (S.L.D.), mschnitz@stanford.edu (M.J.S.)
http://dx.doi.org/10.1016/j.neuron.2015.11.022

SUMMARY

Motor units comprise a pre-synaptic motor neuron and multiple post-synaptic muscle fibers. Many movement disorders disrupt motor unit contractile dynamics and the structure of sarcomeres, skeletal muscle's contractile units. Despite the motor unit's centrality to neuromuscular physiology, no extant technology can image sarcomere twitch dynamics in live humans. We created a wearable microscope equipped with a microendoscope for minimally invasive observation of sarcomere lengths and contractile dynamics in any major skeletal muscle. By electrically stimulating twitches via the microendoscope and visualizing the sarcomere displacements, we monitored single motor unit contractions in soleus and vastus lateralis muscles of healthy individuals. Control experiments verified that these evoked twitches involved neuromuscular transmission and faithfully reported muscle force generation. In post-stroke patients with spasticity of the biceps brachii, we found involuntary microscopic contractions and sarcomere length abnormalities. The wearable microscope facilitates exploration of many basic and disease-related neuromuscular phenomena never visualized before in live humans.

INTRODUCTION

As uncovered 90 years ago, the nervous system controls muscle force generation in a quantal manner by successively recruiting motor units of increasing size (Adrian and Bronk, 1929; Henneman, 1957; Liddell and Sherrington, 1925). The net force depends on the contractile speeds of the excited units' muscle fibers and the lengths of their sarcomeres, striated muscle's basic force-generating elements (Edman, 1979; Gordon et al., 1966). Many movement disorders such as cerebral palsy, myotonic dystrophy, Charcot-Marie-Tooth disease, and myasthenia gravis disrupt motor unit activation, sarcomere structure, or contractile dynamics (Friedrich et al., 2010; Nelson et al., 2013; Pontén et al., 2007; Saporta et al., 2011; Serra et al., 2011; Smith et al., 2011). Motor neuron diseases including amyotrophic lateral sclerosis (ALS), progressive bulbar palsy, and spinal muscular atrophy involve the death of motor neurons (Galea et al., 2001; Manole et al., 2014; Sreedharan and Brown, 2013). Recent data indicate that motor neuron death can also occur in syndromes such as sarcopenia that were originally considered muscle disorders (Drey et al., 2013, 2014). All diseases causing motor unit loss disrupt the neural control of sarcomere contractility.

Despite the devastating nature of many such diseases and the motor unit's physiological importance, to date no imaging technology has allowed observations of individual motor unit dynamics in live animals or humans. This unmet need has stymied efforts to study motor unit attributes across the human lifespan, examine effects of exercise, uncover how motor disorders affect sarcomeres and their dynamics, and identify microscopic biomarkers for assessing neuromuscular conditions. Prior exploratory approaches to intravital measurement of human sarcomere lengths yielded anatomic but not physiologic data, involved instrumentation unsuited for general clinical use, and often required surgery (Llewellyn et al., 2008; Pontén et al., 2007; Smith et al., 2011). For studies of motor unit physiology, an ideal imaging method would allow observations of sarcomere lengths and contractility in striated muscles across the human body, in any posture and without surgery or anesthesia.

To create such a method, we exploited second-harmonic generation (SHG), a nonlinear optical contrast mechanism that arises intrinsically in striated muscle, without exogenous contrast agents (Llewellyn et al., 2008; Plotnikov et al., 2006). Prior studies used tabletop SHG microscopes to image excised muscle samples (Friedrich et al., 2010; Plotnikov et al., 2006; Ralston et al., 2008), and microendoscopes have allowed minimally invasive SHG imaging of sarcomeres in live muscle (Cromie et al., 2013; Llewellyn et al., 2008). However, both SHG microscopy and microendoscopy have required immobile instrumentation on a vibration-isolation table, including a sizable laser (Cromie et al., 2013; Friedrich et al., 2010; Llewellyn et al., 2008; Plotnikov

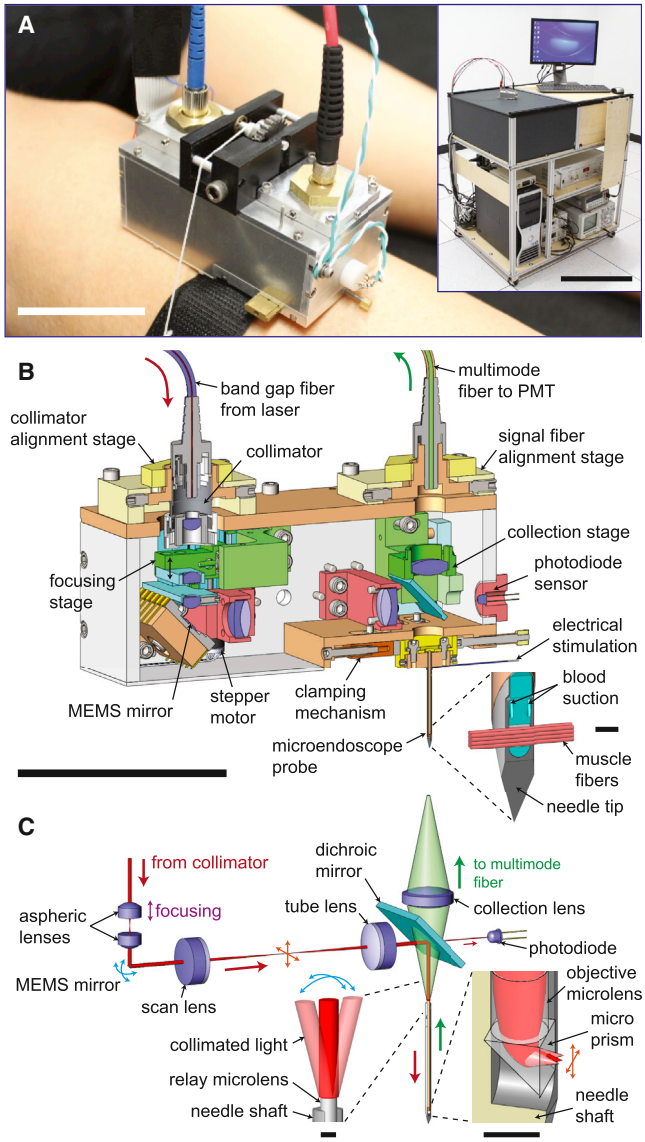

Figure 1. The Wearable Microscope Straps to the Human Body for Imaging Electrically Evoked Motor Unit Twitches

(A) A subject wears the microscope during imaging of the tibialis anterior. Two optical fibers that deliver laser illumination (blue sheath) and collect second-harmonic signals (red sheath) provide flexible optical coupling to a mobile cart. Inset: light source, photodetector, and computer reside on the cart.

(B) Computer-assisted design cross-section of the microscope, showing the housing, optical components, and the electrical line used to excite motor neurons via the microendoscope probe. Inset: magnified view of the probe tip and the muscle fiber orientation during imaging.

(C) Optical pathway in the microscope. Left inset: magnified view of collimated laser beam scanned at three different angles at the back aperture of the microlens assembly. Right inset: laser illumination exiting the micro-prism for the three corresponding scan angles. Cyan arcs and orange arrows indicate Fourier-conjugate planes; rotations about the cyan pivot points correspond to translations in the planes marked orange. Red and green arrows in (B) and (C), respectively, indicate illumination and SHG collection pathways.

Scale bars are 5 cm in (A) and (B), 50 cm in the inset of (A), and 0.5 mm in the insets of (B) and (C).

et al., 2006; Ralston et al., 2008). This has precluded clinical imaging and limited studies to muscles of the forearm, which a subject can insert under the objective lens of an upright microscope (Cromie et al., 2013; Llewellyn et al., 2008). To date, SHG imaging has not revealed single motor unit dynamics.

To study neuromuscular physiology at the level of its fundamental quanta, we designed and built a portable, wearable SHG microscope that can visualize the contractile dynamics of single motor units in nearly any major striated muscle. The microscope uses the intrinsic SHG signals generated by sarcomeres and capitalizes on recent advances in optics by incorporating a photonic crystal optical fiber, a microfabricated laser-scanning mirror, and an ultrafast fiber laser. The entire system resides on a mobile cart. The microscope head fits in the palm of a hand and directly attaches to human subjects, to minimize motion artifacts (Figure 1). For reliable identification of single motor units, the device has a microendoscope probe that enters muscle and electrically excites motor neuron axons.

As we activated motor units via this probe, high-speed image capture of the resulting twitches allowed the first direct visualization of the quantal nature of sarcomere activation in live humans. The time traces of unitary twitches yielded precise determinations of single motor units' contractile speeds. Control studies in mice confirmed that these twitches involved neurotransmission and had the same time course as muscle force generation. Muscle contraction has been well studied at the muscle fiber and motor unit level in animals (Bichler and Celichowski, 2001; Hartree and Hill, 1921) and in some cases humans (Garnett et al., 1979; Sica and McComas, 1971), but had not been directly observed in live human sarcomeres. The capacities to resolve individual motor units, measure sarcomere lengths, and visualize their contractile dynamics will have important implications for research on human neuromuscular physiology and disorders.

RESULTS

Wearable Microscope to Image Striated Muscles across the Human Body

To stimulate motor units and visualize the resulting contractions, we created a mobile instrument comprising a wearable microscope (4.7 cm × 8.8 cm × 3.6 cm), an interchangeable set of multi-functional microendoscope probes for concurrent imaging and electrical stimulation, and an instrumentation cart bearing an ultrafast fiber laser, a photodetector, and electronics (Figure 1A). The design incorporates recent advances in fiber optics, lasers, microlenses, and silicon micromachining to enable a versatile system that can examine contractility in striated muscles throughout the body.

Other than the laser and detector, the microscope integrates all components into one compact unit (Figures 1B and 1C). The laser is Yb^{3+} ion based and delivers dispersion-compensated, ultrashort pulses (~200 fs duration; ~1,030 nm wavelength) to the microscope via a photonic bandgap optical fiber. A microelectromechanical systems (MEMS) laser-scanning mirror, microfabricated in silicon, steers the laser light in two angular dimensions (Figures 1B and 1C). After passing through miniaturized beam steering optics and reflecting off a dichroic mirror, the illumination enters tissue via an "optical needle"

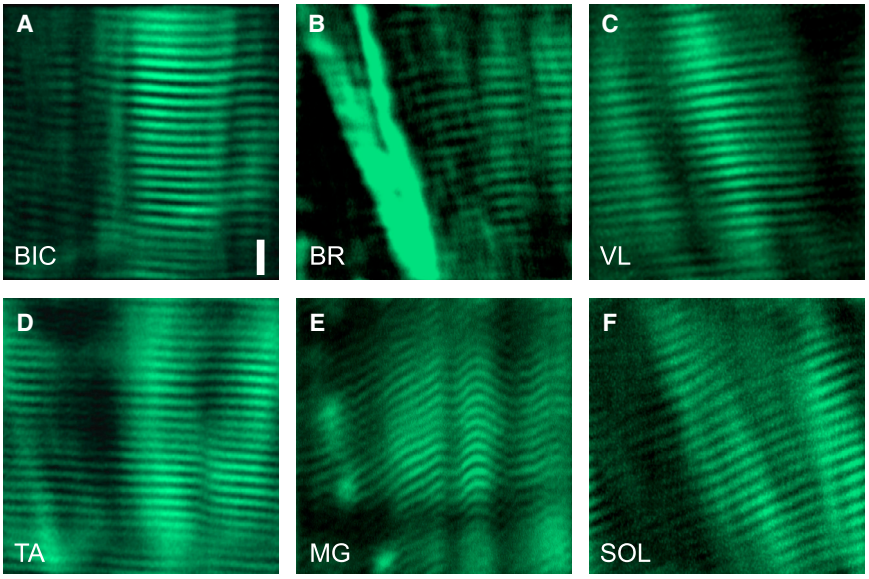

Figure 2. Images of Sarcomeres in a Range of Human Muscles

(A) Image taken in the biceps brachii. The subject had 70° of shoulder abduction, 10° of shoulder flexion, 165° of elbow extension, and the hand pronated with the palm on a flat horizontal surface.

(B) Image taken in the brachioradialis, with 170° of elbow flexion and the hand pronated with the palm on a flat horizontal surface.

(C) Image of the vastus lateralis, with 110° of knee flexion.

(D) Image of the tibialis anterior, with 10° of plantar flexion.

(E) Image of the medial gastrocnemius, with 0° knee and ankle flexion.

(F) Image of the soleus with 0° knee and ankle flexion.

Each of the six images is from a different subject. Images were band-pass filtered to remove background signals while maintaining spatial frequencies corresponding to the physiologic range of sarcomere lengths. Thick diagonal band in (B) is connective tissue.

Scale bar is 10 μm and applies to all panels.

(500-μm-diameter; 19-mm-long) composed of two gradient refractive index microlenses and a microprism (Figures 1B and 1C). SHG signals return through this probe and the dichroic mirror and enter a multimode optical fiber, which routes to a photomultiplier tube on the cart (Figures 1A–1C). The mechanical flexibility of the optical fibers allows patients to comfortably assume postures of biomechanical interest during imaging.

The optical needle has several features to overcome the challenges of intramuscular imaging. The optical pathway is insensitive to the small misalignments that inevitably occur during repeated attachments to the microscope (Experimental Procedures and Figure S1). A microprism at the needle tip (Figures 1B and 1C, insets) provides a side-viewing orientation that allows inspection of several muscle fibers at the same puncture site, simply by adjusting the needle's depth in tissue (Figures S2 and S3). The optical resolution (1.47 ± 0.02 μm FWHM of the lateral point spread function; mean ± SEM), magnification, and illumination power all stay constant as the focal plane is adjusted (Figure S1).

The optical needle is encased in a 20G hypodermic, each of which we created from solid stainless steel wire for use with individual patients. To excite motor units each microendoscope probe has a metal wire connected to the base of its shaft (Figure S2). Each probe also has a solid sharp tip to puncture tissue without coring (Figure S2) and an optical window near the tip (Figures 1B and 1C, insets). The hypodermic's steel shaft is electrically insulated with polyimide, but the metal cutting tip remains bare. Each probe also has a pair of built-in suction tubes to aspirate blood, which otherwise would attenuate optical signals. The microendoscope probe easily detaches from the microscope, for sterilization between usages.

Measurement of Sarcomere Lengths

As a necessary prelude to studies of contractility, we validated our ability to image relaxed sarcomeres in muscles of alert human subjects (Figure 2). We selected six muscles of diverse physiologic attributes and locations—biceps brachii, brachioradialis, vastus lateralis, tibialis anterior, medial gastrocnemius, and soleus—and imaged one muscle from this set in each of six subjects (Figure 2). We first used ultrasound imaging to identify the muscles and their fiber orientation at the microendoscope injection site. To insert the microendoscope rapidly with minimal pain, we built a spring-loaded injector that propels the probe through skin, subcutaneous fat, fascia, and into the muscle while keeping the microprism's external face parallel to the long axes of the muscle fibers. We attached the microscope to the back end of the microendoscope protruding outside the body and strapped it to the subject to minimize motion artifacts (Figure 1A). Subjects reported minimal discomfort, required no anesthesia, and assumed postures that avoided slackening of the muscle under observation.

After these steps, we acquired laser-scanning SHG images (78 μm × 78 μm field of view; 2.1 Hz frame rate) over focal distances 0–150 μm from the prism face. Connective tissues sometimes generated strong SHG signals (Figure 2B); in these cases, we imaged the adjacent sarcomeres by remotely controlled adjustment of the focal plane. Motion artifacts were sufficiently small that it was possible to improve image fidelity by averaging successive frames without computational image registration. Imaging sessions lasted up to ~1 hr but, especially as we gained more experience, usually took 10–15 min to gather the desired data.

We computed mean sarcomere lengths from the image data by finding the fundamental spatial frequency of the sarcomere pattern (Experimental Procedures). This allowed determinations of mean sarcomere lengths as short as 1.5 μm, the limit set by the optical resolution (Figure S1A). The statistical uncertainties in the values of mean sarcomere lengths are in the tens of nanometers, far below the resolution limit. In essence, this precision stems from the ability to count the sarcomeres across a known field

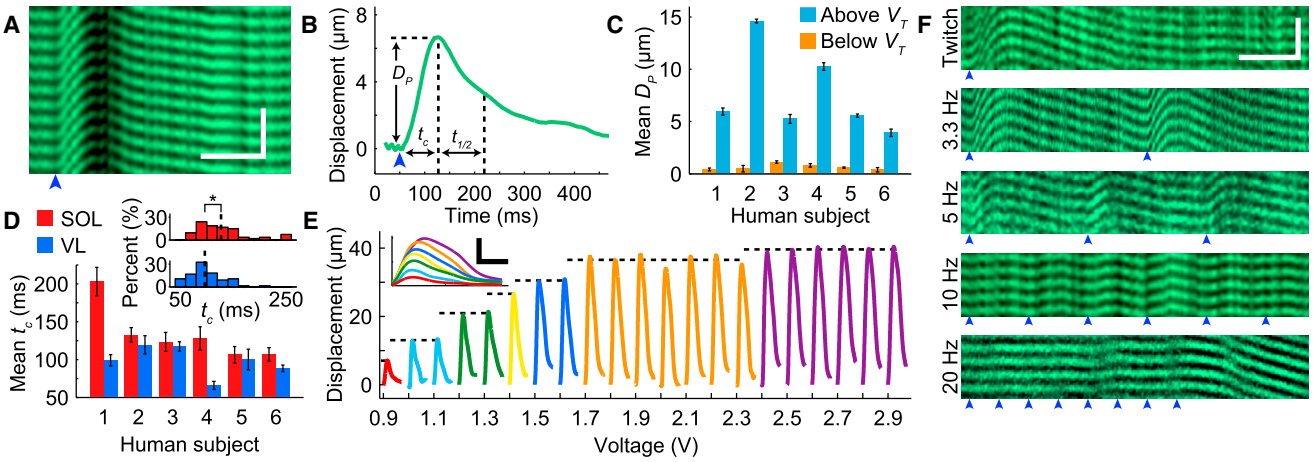

Figure 3. Intramuscular Stimulation and High-Speed Imaging Reveal Contractile Characteristics of Single Motor Units in Human Muscle

(A) A line-scanning image taken during electrical stimulation in the tibialis anterior reveals muscle twitch dynamics. Blue arrowhead marks the onset of a 4 V stimulus. Scale bars are 10 μm (vertical) and 100 ms (horizontal).

(B) Time course of the unitary twitch in (A). Blue arrowhead marks stimulus onset. Dashed horizontal line marks the sarcomeres' peak displacement (D_P). Dashed vertical lines mark the time of peak displacement (t_c) and the subsequent interval over which relaxation to half the peak displacement occurs ($t_{1/2}$).

(C) Unitary twitch contractions occur in an all-or-none manner at a minimum threshold value of electrical stimulation. The plot shows measured values of D_P from six example, individual muscle fibers in the vastus lateralis from six different healthy subjects. V_T denotes the threshold voltage, the minimum stimulation voltage that reliably excited a twitch. We took multiple measurements of D_P using successive stimuli delivered with the imaging needle at a single position in each subject. For voltages just below V_T, there was virtually no discernible twitch (orange bars). Slight increases that raised the voltage above V_T yielded prominent twitches (blue bars), illustrating the all-or-none character of twitch responses around the threshold. Error bars denote SEM (n = 4 measurements per datum).

(D) Mean values of t_c are shorter in vastus lateralis (blue bars) than in soleus (red bars), as measured in the same set of six healthy subjects. We took multiple measurements per subject by evoking unitary twitches at different needle depths in the same injection site (n = 9–24 trials in vastus lateralis and 7–20 trials in soleus). Error bars denote SEM. Inset: histograms of t_c in vastus lateralis and soleus, pooled across subjects. Dashed vertical lines indicate the mean t_c in each muscle. Asterisk denotes the significant difference in mean t_c values between the two muscle types ($p = 7 \cdot 10^{-4}$; Wilcoxon rank sum test; n = 77 and 54 total trials in vastus lateralis and soleus, respectively).

(E) The peak sarcomere displacement (D_P) in vastus lateralis rises in discrete steps as the stimulation voltage increases. Colored traces show displacement versus time curves for unitary (red trace) and non-unitary (other traces) twitches evoked by stimulation voltages indicated by the *x*-axis value at the start of each trace. Each trace is 425 ms in duration, starting with stimulus onset. Each color highlights a set of one or more twitches, evoked at one or multiple voltage levels, but with similar peak displacements and time courses. Dashed horizontal lines mark the mean peak displacement in each set. No twitches occurred for stimulation voltages below 0.9 V. Inset: superposition of the average time courses for each set. Scale bars in the inset are 20 μm (vertical) and 100 ms (horizontal).

(F) Line-scanning images acquired during trains of electrical stimuli to the posterior deltoid using different stimulation frequencies. The measured t_c value of the muscle fiber (71 ms) predicts substantial twitch summation at a frequency ($1/t_c$) of ~14 Hz. In response to an isolated stimulus there is an individual twitch (top). Successive twitches sum during 3.3-Hz to 20-Hz-stimulation, with smooth sustained contraction at 20 Hz. Blue arrowheads mark stimulus onsets. Scale bars are 10 μm (vertical) and 100 ms (horizontal).

of view. For instance, a count of 100 sarcomeres across a 350-μm-diameter field bounds the mean sarcomere length within 3.47–3.54 μm, even before image details are analyzed. At individual injection sites, we determined mean sarcomere lengths in relaxed muscle of 3.10 ± 0.04 μm (biceps brachii), 3.25 ± 0.05 μm (brachioradialis), 3.13 ± 0.02 μm (vastus lateralis), 2.88 ± 0.01 μm (tibialis anterior), 3.16 ± 0.02 μm (medial gastrocnemius), and 3.01 ± 0.02 μm (soleus) (mean ± SEM; one image per subject; 50 sarcomeres analyzed per image; Figures 2A–2F), indicating ~10–50 nm measurement precision.

To gauge inter-subject variability, we studied the calf muscles, medial gastrocnemius and soleus, in more detail. Subjects sat on a padded table with knee and ankle at 0° of flexion. During imaging we varied the optical needle's insertion depth to allow different muscle fibers to enter the field of view (Figure S3). For each subject, we calculated a muscle's mean sarcomere length as the average across all visualized fibers. The mean value in gastrocnemius across individuals was 3.09 ± 0.1 μm (mean ± SD; n = 3 subjects); in soleus, it was 3.15 ± 0.31 μm (n = 5 subjects). Hence, compared to our measurement precision of ~30 nm, inter-subject variability in mean sarcomere lengths was in the ~100–300 nm range, or <10% of mean length values.

In Vivo Imaging of Contractile Dynamics

Having validated measurements of sarcomere lengths, we next studied motor unit contractility evoked by electrical stimulation via the microendoscope's metal sheath (Figures 3A–3F). Stimulation involved one or more negative-going voltage pulses lasting 200 μs, of tunable frequency and magnitude. To excite motor neuron axons, rather than directly evoking muscle action potentials, we limited stimulation to several volts or less (maximum 6 V). Prior studies have shown that low-voltage intramuscular stimulation activates motor neurons, not muscle fibers, and that the voltages needed to directly excite muscle fibers are 1–2 orders of magnitude greater than those used here (Hultman et al., 1983; Muir and Lemon, 1983; Taylor and Stephens, 1976).

To observe contractile responses, during stimulation we recorded line-scanning images by sweeping the laser focus back

and forth at 1.09 kHz along a line perpendicular to the muscle striations (Figures 3A and 3B). We began experiments by incrementally increasing the stimulus voltage from 0 V until the first appearance of a twitch. We then fine-tuned the stimulus in 0.01 V increments to find the lowest voltage that produced an observable contraction. At every imaging site in all subjects, we found there was a minimum, threshold stimulation voltage necessary to evoke a twitch. The exact value of this threshold, V_T, varied by hundreds of millivolts from site to site, but there was always a twitch response to any stimulus that exceeded the local value of V_T. For example, in the vastus lateralis of healthy human subjects, the peak sarcomere displacement, D_P, was abruptly larger for stimulus levels just above V_T versus those just below V_T (Figure 3C). When the voltage crossed V_T there was a sudden rise in D_P magnitudes, from 0.63 ± 0.09 μm to 7.59 ± 0.78 μm (mean ± SEM; n = 6 subjects, 4 pre-threshold and 4 post-threshold trials per subject; $p = 3 \times 10^{-9}$; Wilcoxon rank sum test) (Figure 3C). These observations fit with the need to excite at least one motor unit to see an evoked contraction.

At the threshold voltage, the sarcomeres' maximal displacements were typically <15 μm. Our subjects did not perceive these contractions, and we saw no motion of the skin or limb, presumably because one motor unit comprises a small fraction of a muscle's fibers. After extracting twitch time courses from the sarcomere displacement images, we determined the contraction and half-relaxation times, t_c and $t_{1/2}$, which respectively denote the rise time from stimulation onset to the time of sarcomeres' peak displacement, D_P, and the decay time from this peak to 50% of D_P (Figures 3A and 3B).

Sarcomeres exhibited almost no shortening during stimulation, despite their obvious displacements across the images. Across entire rows of sarcomeres in line-scan images, we compared mean sarcomere lengths during a twitch (0, t_c) to the mean after the contraction was done (>3t_c) (n = 26 contractions in 3 subjects). The declines in sarcomere length during muscle activation were significant (–0.04 ± 0.01 μm; mean ± SEM; p = 0.04; Wilcoxon signed rank test) but <1.5% of the sarcomere lengths. This is not surprising, since a stimulus that recruits only one motor unit should induce a tiny fraction of the muscle's maximal contraction. To support this interpretation, it was crucial to verify that the twitch time course reflected that of muscle force generation and that the twitches we evoked reflected motor neuron activation.

Evoked Twitches Report Muscle Force Generation and Require Neurotransmission

To verify that the twitches evoked by our microendoscope reflect muscle force generation, we applied our imaging protocol in anesthetized mice. This allowed concurrent measurements of muscle force production in a way that was infeasible in humans. To track both force and sarcomere dynamics, we stimulated the gastrocnemius via the microendoscope (n = 3 mice; 7 injections per mouse; 10 twitches per injection) while monitoring twitch force via a transducer attached to the Achilles tendon (Figures 4A and 4B).

As in human studies, our probe stimulated only a fraction of the muscle. By measuring the maximum force each gastrocnemius could produce (Experimental Procedures), we found that individual twitch forces were 0.6%–10% of the maximum. Further, the temporal waveforms for each fiber's evoked force and sarcomere displacements were nearly identical (Figure 4B). This similarity held for fibers with a range of contraction times (19–30 ms) and led to excellent agreement between values of t_c and $t_{1/2}$ determined from the two measurement types (r = 0.96 and 0.89, respectively, for t_c and $t_{1/2}$) (Figures 4C and 4D). This close correspondence between the two measurement modalities confirmed that image-based characterizations of sarcomere twitch dynamics accurately reflect the time course of twitch force production.

We also used anesthetized mice to verify that the evoked twitches arose from excitation of motor neurons, not direct elicitation of muscle action potentials (n = 3 mice). We confirmed the pre-synaptic locus of excitation by administering atracurium besylate, a neurotransmission blocker (Bowman, 2006), while imaging twitches in the gastrocnemius. Drug delivery eliminated twitching despite continued muscle stimulation (Figures 4E and 4F). Thus, twitches evoked by the microendoscope require neurotransmission and involve motor neuron activation, in agreement with past studies of intramuscular stimulation (Hultman et al., 1983; Muir and Lemon, 1983; Taylor and Stephens, 1976).

Determinations of Motor Unit Contractile Speeds

The characteristic time in which a muscle fiber performs a twitch, t_c, is one marker of motor unit type (Burke et al., 1971; Garnett et al., 1979; Sica and McComas, 1971). The wearable microscope provided a first opportunity to track the contractile dynamics of single motor units in healthy humans and muscles with varying proportions of different motor unit types. We compared t_c values in the vastus lateralis and soleus muscles of six healthy subjects. Soleus has mainly slow motor units, whereas vastus lateralis has a mix of fast and slow types (Edgerton et al., 1975; Gollnick et al., 1974). Indeed, unitary contractions in soleus had significantly slower rise times (Figure 3D). Mean t_c values were 99 ± 4 ms and 127 ± 6 ms, respectively, in vastus lateralis and soleus (mean ± SEM; n = 6 subjects, 77 trials in vastus lateralis and 54 in soleus; $p = 7 \times 10^{-4}$; Wilcoxon rank sum test). However, t_c values ranged widely (40–218 ms in vastus lateralis; 64–251 ms in soleus; Figure 3D, inset), in agreement with past studies of human motor units and muscle fibers (Eberstein and Goodgold, 1968; Garnett et al., 1979; Sica and McComas, 1971).

The range of measured contraction times shows our protocol can recruit motor units of fast and slow varieties and yields an indication of muscle fiber type composition. Consistent with this, when the microendoscope was held fixed in vastus lateralis, gradual increases in stimulation voltage yielded quantal increases in peak sarcomere displacements with clear, stepwise transition thresholds (Figure 3E, inset). The temporal waveform of the sarcomere displacements changed abruptly at these stimulus thresholds, consistent with addition of successive motor units of varying speeds.

Summation of Multiple Twitches into Sustained Contractions

After imaging unitary twitches in temporal isolation, we explored in one subject whether we could see summation of multiple

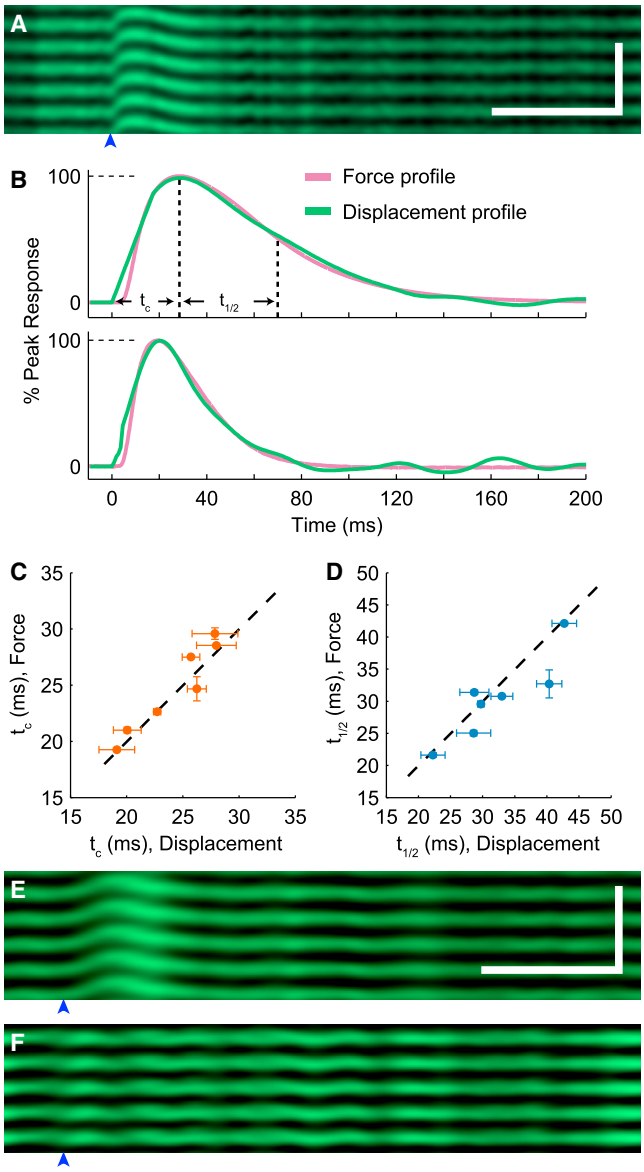

Figure 4. Sarcomere Displacement and Twitch Force Exhibit Nearly Identical Dynamics

(A) A line-scanning image taken in the medial gastrocnemius of a live mouse during an evoked twitch shows the time course of sarcomere displacement. Blue arrowhead marks the stimulus onset. The empirically determined t_c and $t_{1/2}$ values are 26.6 ± 0.1 ms and 29.6 ± 0.4 ms, respectively (mean ± SEM). Scale bars are 10 μm (vertical) and 100 ms (horizontal).

(B) Normalized time courses of sarcomere displacement and twitch force development during an evoked contraction have nearly identical waveforms. The two measurements show strong agreement for a slow twitch (upper trace, t_c and $t_{1/2}$ are 28.5 ± 0.1 ms and 42.1 ± 0.1 ms, respectively; mean ± SEM) and a faster twitch (lower trace, t_c and $t_{1/2}$ are 19.3 ± 0.2 ms and 21.6 ± 0.4 ms, respectively) as recorded from separate injections in the same mouse.

(C) Contraction times, t_c, determined from the time of peak sarcomere displacement are nearly identical to t_c values measured directly from the force time course in the tendon (r = 0.96; n = 3 mice, 7 injections, 10 trials per injection). Error bars in (C) and (D) denote SEM. Diagonal dashed lines mark the line of equality, $y = x$.

(D) Half-relaxation times, $t_{1/2}$, measured from the decay of sarcomere displacement, show a strong correlation and near identical values with $t_{1/2}$ measured directly from the tendon force (r = 0.89; n = 3 mice, 7 injections, 10 trials per injection).

(E and F) Twitch contractions in a mouse medial gastrocnemius visualized in (E), disappear in (F) after blockade of neuromuscular transmission by administration of atracurium besylate. Blue arrowheads mark stimulus onset. Scale bars are 10 μm (vertical) and 100 ms (horizontal).

twitches into sustained contractions. While activating one motor unit with either isolated or trains of stimuli delivered at 3.3, 5.0, 10 or 20 Hz, we acquired line-scan images in the posterior deltoid (Figure 3F). In this subject, t_c and $t_{1/2}$ values for single twitches were 71 ± 4 ms and 117 ± 8 ms, respectively (mean ± SD, n = 5 contractions). This t_c value is within the typical range (35–140 ms) for human muscle (Eberstein and Goodgold, 1968; Sica and McComas, 1971) and predicts initiation of twitch fusion at a frequency ($1/t_c$) of about 14 Hz. Our observations fit this prediction well. During 3.3-Hz-stimulation, we observed some summation between successive twitches (Figure 3F). Stimuli between 5 Hz and 20 Hz induced further twitch summation and smoothing of the sustained contraction. At 20-Hz-stimulation, contractile oscillations were no longer visible (Figure 3F). As during imaging of single twitches, there was minimal sarcomere shortening and contractions were imperceptible to our subjects. The ability to observe such phenomena opens new opportunities to examine conversion of electrical signals into muscular action.

Sarcomere Dynamics in Spastic Muscle of Post-stroke Patients

We expect the wearable microscope to facilitate studies of human neuromuscular diseases and disorders. To illustrate, we imaged sarcomeres in the biceps brachii muscles of patients with spasticity secondary to hemiplegic stroke. How spasticity affects sarcomere anatomy and dynamics is unknown as there has been no way to visualize sarcomeres in post-stroke survivors. Notably, the spasticity diagnosis typically does not distinguish patients with involuntary, sustained contractions from those with permanent changes in sarcomere lengths (or combinations thereof).

We collected static and dynamic images of sarcomeres in spastic muscle and compared these to images from the contralateral arm in the same subjects (n = 4 patients). We rested subjects' arms on a flat surface and imaged multiple fibers in each biceps brachii with the same posture for both arms. Although subjects attempted to relax their muscles, in the affected arms we observed intermittent involuntary fasciculations and sustained contractions (Figures 5A and 5B). Line-scanning images revealed ongoing unfused contractions in spastic muscle (Figure 5A) that were not present in the contralateral muscle (Figure 5B).

We also compared sarcomere lengths in the spastic and contralateral biceps. The affected and contralateral muscles both exhibited uniform sarcomere morphology but had plain differences in sarcomere spacing (Figures 5C and 5D). The patients had significant differences in sarcomere lengths between the two biceps (absolute length differences of 0.48 ± 0.11 μm; mean ± SEM; n = 4 post-stroke subjects) that were not present

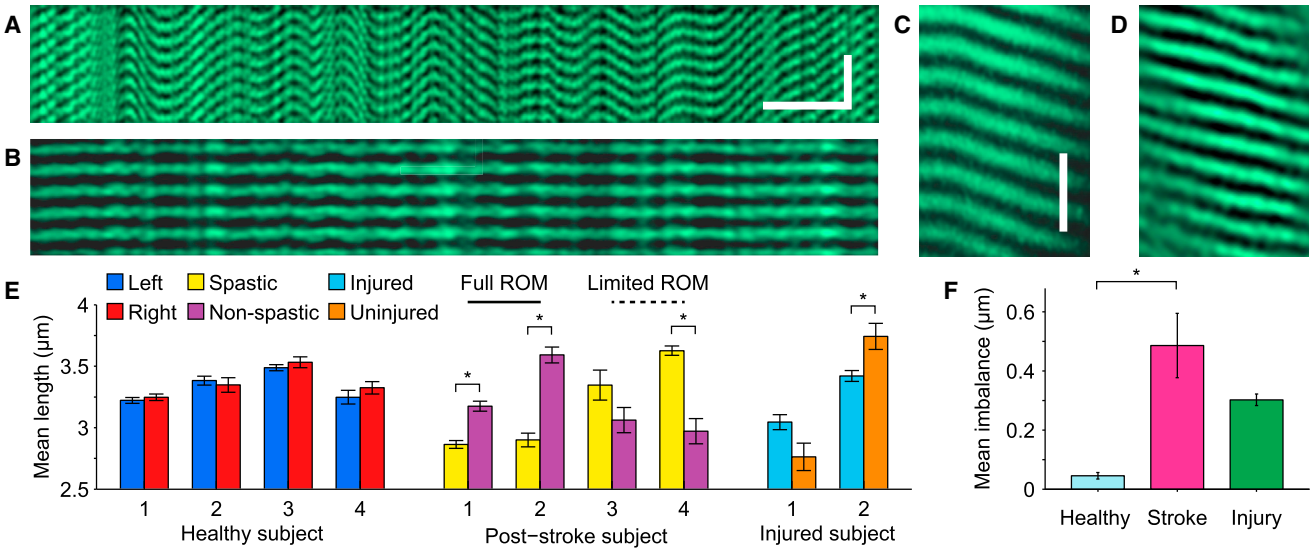

Figure 5. Post-stroke but Not Post-injury Patients Exhibited Microscopic Contractions in the Biceps Brachii, whereas Both Groups Had Bilateral Asymmetries in Sarcomere Lengths

(A) Line-scanning image taken in the biceps brachii of the relaxed, affected limb of a post-stroke subject reveals sustained, micron-scale involuntary contractions in the imaged sarcomeres. The frequency of the unfused tetanus was approximately 11.5 Hz. Scale bars are 10 μm (vertical) and 100 ms (horizontal) and also apply to (B).

(B) Line-scanning image in the unaffected limb of the same subject as in (A) shows no involuntary contractions.

(C and D) Sarcomeres in the affected biceps of a post-stroke patient, (C), are longer (3.74 ± 0.02 μm; mean ± SEM) than sarcomeres in the unaffected, contralateral biceps (2.90 ± 0.01 μm), (D). Scale bar is 10 μm and applies to both panels.

(E) Comparisons of sarcomere lengths in the biceps brachii of both arms of healthy subjects, post-stroke patients, and post-injury patients (n = 4, 4, and 2 subjects, respectively). Error bars denote SEM (n = 9–13 measurements in healthy right arms and 8–14 measurements in healthy left arms; n = 4–9 measurements in spastic arms of stroke subjects and 3–8 measurements in non-spastic arms of stroke subjects; n = 11 and 8 measurements in injured arms and 4 and 5 measurements in uninjured arms, respectively). Post-stroke patients had significantly different sarcomere lengths between the spastic and non-spastic biceps. Asterisk denotes $p < 0.05$ (Wilcoxon rank sum test). Patients whose arm retained the full range of motion (ROM) had shorter sarcomeres in the spastic arm; those with impaired ROM had longer sarcomeres in the spastic arm.

(F) The absolute value of the mean difference in sarcomere lengths between the two biceps brachii of post-stroke patients differed significantly from that of healthy subjects. Asterisk denotes $p = 0.03$ (Wilcoxon rank sum test). Error bars denote SEM.

in approximately age-matched healthy individuals (0.05 ± 0.01 μm; mean ± SEM; 4 control subjects; $p = 0.03$, Wilcoxon rank sum test) (Figures 5E and 5F). Although each post-stroke patient had differences in sarcomere lengths that were substantially greater than seen in any of the control subjects, the sign of this effect differed between patients who retained a full range of motion and those who did not (Figure 5E). This consistent disruption in sarcomere length but of a variable sign points to the potentially divergent adaptations that may occur in muscles afflicted by contracture or spasticity secondary to stroke. Suitable treatments might depend on whether the sarcomeres are longer or shorter than normal.

As a negative control group against which to compare the stroke patients, we examined two orthopedic patients who had suffered musculoskeletal injury to the biceps brachii muscle or glenohumeral joint but had no diagnosed neurologic deficits. We hypothesized that while orthopedic patients might exhibit anatomic abnormalities in sarcomere lengths, unlike neurology patients they should not display abnormal neuromuscular signaling. The data bore out these expectations; each orthopedic subject exhibited sarcomere length differences across the two arms greater than in any of the healthy subjects (Figure 5E). But unlike post-stroke patients, the orthopedic patients showed no fasciculations or other involuntary microscopic contractions. Hence, the physiologic irregularities seen in post-stroke patients were likely specific consequences of the impairments to motor control, not generic consequences of muscle damage. Overall, the wearable microscope's capacities to reveal anatomic and physiologic abnormalities in live muscle showcase its potential to broaden understanding of a wide range of neuromuscular disorders.

DISCUSSION

The wearable microscope allows precise measurements of sarcomere lengths and contractile dynamics in alert humans. Unlike traditional endoscopy, which is well suited for imaging in natural body cavities or those created intra-operatively, our instrument's microendoscope works well in solid tissue and is propelled into the body in a fraction of a second. The microscope's mobility (Figure 1A, inset), versatility (Figure 2), and minimally invasive capabilities allow new types of observations (Figures 3, 4, and 5) for medical research and clinical imaging of patients with movement disorders. Beyond muscle, the microscope should allow in vivo imaging of multiple tissues previously examined in vitro using SHG contrast, including skin, cartilage,

tendon, bone, and tumors (Campagnola, 2011; Chen et al., 2012). The technological advances reported here should also apply to other forms of nonlinear optical contrast, such as coherent anti-Stokes Raman scattering, two-photon excited fluorescence, third-harmonic generation, and stimulated Raman scattering, which all show promise for tissue inspection but have been nearly prohibitive to deploy clinically due to the challenges of miniaturization (Flusberg et al., 2005).

Our procedures were well tolerated in adult patients and enabled detailed comparisons to healthy subjects. Nevertheless, our approach has limitations. Measurements taken at varying joint angles require removal of the probe between postural changes since the rigid needle impedes muscle motion. The needle also impedes large contractions that would otherwise yield substantial translation of muscle beneath the skin. For now, these constraints preclude studies in subjects executing large, dynamic motions. However, we readily examined single motor unit contractions that did not introduce artifacts.

Comparisons to Prior Measurements of Human Sarcomere Lengths

To date, nearly all data on human sarcomere lengths have been acquired in chemically fixed cadavers, and potential inaccuracies introduced by fixation and rigor mortis have long been discussed (Arnold et al., 2010; Cutts, 1988; Ward et al., 2009). However, in vivo measurements of sarcomere lengths in the forearm extensor carpi radialis brevis taken with laser diffraction methods agree well with those attained using a tabletop form of SHG microendoscopy (Cromie et al., 2013). We compared our in vivo measurements to predictions from a musculoskeletal model based on extensive data from 21 cadavers (Arnold et al., 2010). At the postures studied here, the model predicts sarcomere lengths of 3.71 μm in vastus lateralis, 2.99 μm in tibialis anterior, 3.16 μm in medial gastrocnemius, and 2.80 μm in soleus (Figure 2). Our values from live humans are respectively within –16%, –4%, –2%, and +12% of these predictions. These differences approach the ~10% variability in mean sarcomere lengths that we observed between different subjects. Overall, by enabling direct observations in live subjects, the wearable microscope provides the ability to circumvent the inaccuracies of cadaver studies.

Visualization of Muscle Twitch Dynamics

Nearly all sarcomere movements during electrically evoked twitches were translational displacements, not sarcomere shortening. The slight shortening we saw likely resulted from stretching of nearby passive structures (inactive muscle fibers and connective tissue) between the needle and the nearest tendon. The probe's imaging window is ~0.5 mm from the needle edge, where the muscle fiber is pinned on the needle. Over this 0.5 mm span an ~1.5% sarcomere shortening should yield a net sarcomere displacement of 7.5 μm. This agrees well with the measured mean twitch displacement of 7.6 ± 0.8 μm (Figure 3C). Unlike supramaximally stimulated muscle in which substantial tendon stretch causes timing differences between fascicle shortening and force production (Griffiths, 1991), our evoked contractions are much smaller, usually engage only one motor unit, and display nearly identical timing for sarcomere displacements and force production (Figure 4). The wearable microscope thus provides direct information about force-generation speeds and individual fiber types.

However, we were unable to acquire useful data during subjects' voluntary contractions, which caused substantial motion artifacts that made imaging prohibitive. Even healthy subjects could not reliably produce small, controlled contractions. Further, voluntary contractions typically involve multiple motor units. Thus, any twitch speeds we might have determined from voluntary contractions would have reflected activation of an unknown mixture of fast and slow fiber types, complicating interpretation. Finally, whereas muscle recruitment in voluntary contractions favors slow motor units (Henneman, 1957), intramuscular stimulation excites motor units near the stimulation needle and thus provides a more accurate and unbiased sampling of the muscle's fiber type composition.

Clinical Applicability of Sarcomere Length Measurements

Ex vivo studies of diseased or aged muscle tissues have identified altered sarcomere structures, extracellular matrix, and contractile properties (D'Antona et al., 2003; Friedrich et al., 2010; Plotnikov et al., 2008; Ralston et al., 2008). Clinical methods based on in vivo imaging of these features have awaited an imaging modality suitable for routine use in patients. The wearable microscope meets this need through minimally invasive imaging of live sarcomeres, without surgery or anesthesia, in nearly every skeletal muscle and postural position.

In addition to disease diagnosis and monitoring, our technology may yield improvements in surgical planning and practice. Surgical treatments of abnormal gait patterns are often unsuccessful (Hicks et al., 2011), possibly due to sub-optimal sarcomere operating lengths in the healed muscles. In children with cerebral palsy, it is often difficult to identify which muscles are disrupting the gait pattern. Surgeries to alter muscle or tendon lengths are performed without intra-operative means to assess sarcomere lengths. Sarcomeres that are too short do not produce sufficient force (Gollapudi and Lin, 2009) and can result in severe postoperative muscle weakness (Delp et al., 1995; Sammarco et al., 2006). Sarcomeres that are too long generate excessive passive forces that restrict motion (Pontén et al., 2007; Smith et al., 2011). Studies of muscle adaptation after surgery may be vital to optimize surgical treatments of conditions such as cerebral palsy, spasticity and strabismus. Our microscope makes such studies possible in living patients.

In post-stroke patients, we found significant differences in sarcomere lengths between the spastic and contralateral arms in all patients examined. Intriguingly, the patients with full range of motion through the elbow had shorter sarcomere lengths in the spastic limbs, whereas patients without the full motion range had longer sarcomeres in their spastic limbs. A larger study would be required for definitive conclusions, but abnormally long sarcomeres are consistent with muscle contracture (Pontén et al., 2007; Smith et al., 2011) and could explain the excessive tightness in these two subjects. These results speak to our technology's ability to provide specific measurements of sarcomere lengths and contractile dynamics, which may help reveal which

muscles are abnormal and likely culprits impeding patients' movement.

Clinical Applicability of Monitoring Individual Motor Units

Our studies under blockade of neurotransmission indicate that our intramuscular stimulation protocol recruits motor neurons, and not muscle fibers directly. Activation of motor units occurred in a discrete fashion and required the stimulation voltage to exceed a minimum threshold value (usually near 1 V) for excitation of the first motor unit (Figures 3C and 3E). In patients with motor neuron disease, present methods for assessing motor unit loss and re-innervation rely on electromyography (EMG) signals evoked by nerve stimulation. Due to the indirect way in which these signals relate to force generation and the difficulties in interpreting them for large muscles, EMG-based assessments of motor unit loss are usually limited to small muscles of the hand or foot (Nandedkar et al., 2010; Shefner et al., 2011). The wearable microscope offers an opportunity to examine motor units in larger muscles, such as those used for balance and gait. This might alleviate the need for EMG and supra-maximal nerve stimulation in hand muscles, which are rich with sensory nerves that make such studies uncomfortable for patients.

More broadly, the ability to characterize single motor units in humans paves the way to diagnostics and biomarkers for neuromuscular diseases that alter motor unit physiology, such as ALS, sarcopenia and spinal muscular atrophy (Drey et al., 2013, 2014; Galea et al., 2001; Nandedkar et al., 2010; Shefner et al., 2011; Sreedharan and Brown, 2013), and those such as myotonic dystrophy that alter the fundamental contractile mechanism (Logigian et al., 2010). In post-stroke patients, we found involuntary microscopic contractions and fasciculations. Future studies of other disorders using our technology will likely uncover other contractile abnormalities. Both neuromuscular disorders and aging can differentially affect motor units of different contractile speeds (Ciciliot et al., 2013; Rose et al., 1994; Vandervoort and McComas, 1986), and such knowledge might inform judgments about disease characteristics and progression. By allowing observations of single motor unit contractions in live humans, the wearable microscope is poised to impact the study, diagnosis and treatment of many motor disorders.

EXPERIMENTAL PROCEDURES

Human Subjects

The Stanford Institutional Review Board approved all procedures, following FDA guidelines (21 CFR 50).

Healthy Subjects

Seven males and five females (ages 23–52 years) gave informed consent for studies of skeletal muscle.

Post-stroke Subjects

We obtained informed consent from four post-stroke subjects (two male, two female, 49–69 years) with spastic hemiplegia secondary to stroke and major impairment of the upper extremity, including spastic elbow flexors. In subjects with dominant hemisphere strokes with any aphasia, we obtained informed consent from the patient and primary caregiver.

Subjects had received different diagnoses for range of motion at the elbow. Subject 1 could attain a full range of motion when stretched slowly. Subject 2 had full passive and active range of motion. We designated these two subjects as having full range of motion. Subjects 3 and 4 were much stiffer and designated as having limited range of motion. For subject 3, full elbow extension was very difficult. In subject 4, extension was limited to 135°.

Age-Matched Healthy Controls

For comparisons with spastic subjects we obtained informed consent from four approximately age-matched individuals (three male, one female, ages 40–53). All subjects reported no prior injury to the biceps brachii in both arms.

Post-injury Subjects

We obtained informed consent from two subjects with injuries to the biceps brachii muscles and associated joints of one arm at least one year prior to imaging. The first (male age 60) fractured a clavicle two years prior to imaging and had substantial asymmetry in resting shoulder posture compared to the healthy limb after recovery. The second subject (male age 85) suffered a full tear of the proximal tendon of the biceps brachii long head 20 years prior to imaging. The tendon was unrepaired, leaving the muscle belly in a shortened position.

For comparisons of sarcomere lengths in the biceps brachii between limbs and subject groups, we secured all limbs to a table with custom fixtures in the same posture: 70° of shoulder abduction, 10° shoulder flexion, 130°–165° elbow flexion, and with the hand pronated with the palm on the tabletop surface. For subjects with limited elbow extension, we secured the injured/spastic limb at the maximum extension and matched the angle on their opposite limb. We used these angles for all subjects regardless of resting postures; sometimes this necessitated stretching and securing the limbs against some baseline tension in the muscles and or joints. We used images of multiple fibers in each injection to calculate a mean sarcomere length.

Animal Subjects

Procedures followed NIH guidelines and were approved by the Stanford APLAC. For comparisons of sarcomere displacements and force dynamics, we used male C57BL/6 mice (mean age 42 days; ~39 g mass). For studies with atracurium besylate, we used female C57BL/6 mice (1–4 months old; ~25 g).

Optical System

A Yb^{3+}-ion-based fiber laser on the imaging cart emitted ultrashort pulses (1,030 nm center wavelength; ~200 fs duration). The laser beam exited the laser with a linear polarization, passed through a half-wave plate and was focused into an air-core band-gap optical fiber (2 m length; NKT Photonics) by an aspheric lens. The band-gap fiber delivered the illumination to the wearable microscope. We compensated for group velocity dispersion in the band-gap fiber using a grating-based pre-chirper placed between the laser and the fiber. Since the fiber partially preserved the linear polarization of the laser light, rotation of the half-wave plate caused a corresponding alteration of the illumination polarization at the sample, thereby allowing the user to alter the polarization and maximize SHG signals from muscle fibers.

Light exiting the band-gap fiber entered a collimator, passed through a focusing stage and reflected off a MEMS dual-axis scanning mirror (Mirrorcle Technologies). The beam then passed through scan and tube lenses, reflected off a short-pass dichroic mirror and entered the back aperture of the optical needle (Figure 1C). Rotations of the scanning mirror pivoted the beam about this back aperture. A photodiode (Figures 1B and 1C) collected a small fraction of the laser light passing through the dichroic mirror, providing a readout of illumination power at the sample. SHG signals collected by the microendoscope returned back through the dichroic mirror. A singlet lens coupled these signals into a multimode fiber (0.22 NA; 910-μm-diameter core) that delivered the photons back to the cart. Photons exiting the collection fiber passed through a fluorescence filter before entering a photomultiplier tube (Hamamatsu; H7422-40). We controlled laser-scanning imaging using custom software programmed in C#.

The microscope's focusing mechanism comprised a pair of aspheric lenses that served as an adjustable telescope (Figure 1C). By using a stepper motor to translate the lens closer to the band-gap fiber, we altered the convergence or divergence of the telescope's outgoing beam and thereby adjusted the focal plane in the specimen. The other aspheric lens was positioned one focal length away from the MEMS mirror (Figure 1C). This yielded a near linear relationship between the position of the focusing lens and the focal distance in tissue. It also allowed the waist of the laser beam to remain unchanged at the back

aperture of the optical needle across the focusing range. Across the entire range, power variations at the sample were <10%, and lateral and axial resolutions were respectively 1.47 ± 0.02 μm and 16.0 ± 1.07 μm (mean ± SEM; Figure S1).

Optical Needles

The 0.5-mm-diameter microlens assembly comprised a 0.2 NA gradient refractive index (GRIN) relay lens, a 0.4 NA GRIN objective lens and a 0.5-mm right-angle prism (GRINTech GmbH). By adjusting the microscope's internal focusing stage, we altered the distance from the prism face to the focal plane in the sample between 0–150 μm (in H_2O). The optical needle focused the collimated light entering its back aperture to a spot in the sample. This ensured imaging was robust to modest misalignments when the optical needle was attached to the microscope. The collimated beam overfilled the back entrance of the relay microlens, thus translational misalignments between the optical needle and microscope induced little image distortion. Angular misalignments led to a displacement of the imaged region in the specimen.

We created a telecentric design by imaging the MEMS mirror onto the back focal plane of the GRIN objective lens, which ensured the image magnification was nearly constant over the entire focal range, essential for accurate length measurements at varying focal distances (Figure S1C). We optimized the laser spot size and Strehl ratio across a field of view 120 μm in diameter by adjusting the refractive index profile of the GRIN lenses (Barretto et al., 2009).

Microendoscope Probes

Unlike prior uses of optical needles that required a separate guide tube to access deep tissues (Barretto et al., 2009; Llewellyn et al., 2008), we fixed our optical needles in a sharpened hypodermic for direct puncturing of tissue. We fabricated hypodermics from solid steel wire and shaped a multi-faceted cutting tip for rapid puncturing of tissue and minimal pain for the subject (Figure S2). The hypodermic had a central cavity into which we inserted the optical needle, as well as suction lines for removing blood from the imaging field. The base of the microendoscope probe had a suction connector, for use with an external vacuum source to remove blood. Suction lines terminated near the microprism, with smoothed edges to prevent coring of tissue or clogging during insertion.

We soldered an insulated stainless steel wire to the base of the metal needle to allow intramuscular electrical stimulation (Figure S2). We secured all components of the microendoscope probe in a polyimide sheath and cemented the assembly with high temperature resistant epoxy (Henkel Loctite) that we tested successfully for up to 10 autoclave cycles.

Imaging Procedures

We cleaned microendoscope probes in an ultrasonic cleaner and sterilized them in an autoclave. We cleaned the microscope's exterior with ethanol. Subjects lay or sat on a padded table. We determined a posture for the subject and a position and orientation of the microscope in which it could rest on the body without applying substantial torque to the injected microendoscope.

Using palpation and ultrasound imaging we identified the muscle and aligned the microscope's fast-scanning axis to the long axes of the muscle fibers. After marking the imaging site and sterilizing the skin, we inserted the microendoscope with a custom spring-loaded injector, such that the external face of the microprism was parallel to the muscle fibers' long axes. Even with slight alignment errors, the compliance of the fibers allows them to maintain a parallel contact on the face of the microprism. After injecting the microendoscope, we attached the wearable microscope to the probe and secured the microscope to the subject with velcro strapping. We asked subjects to relax the muscle and hold still; we then took imaging data for up to 1 hr, but more commonly 10–15 min. To improve our statistical power while minimizing the number of injections per subject, we used a custom translation stage to examine muscle fibers at different depths from the skin.

Visualization of Twitches

We induced twitches by intramuscular stimulation through the microendoscope probe's metal sheath. After inserting the probe and connecting the microscope, we connected the stimulation wire to a custom pulse-generating circuit. We fixed a grounding pad to the skin near the injection site. Stimulation comprised negative-going voltage pulses, 200 μs in duration, of tunable frequency and magnitude. We took line-scanning images of activated tissue with the scanning and muscle fiber axes aligned. We incrementally increased the pulse voltage until the first appearance of a twitch. We adjusted the stimulus in 0.01 V increments to reach the lowest voltage causing an observable displacement. The voltage needed to excite the smallest twitch varied considerably between injection sites and individuals but was typically between 1–6 V. To study un-fused tetanus, we delivered pulse trains of constant magnitude at 0, 3.33, 5, 10 and 20 Hz.

Analysis of Sarcomere Lengths

We determined mean sarcomere lengths as the fundamental spatial frequency of the periodic sarcomere pattern along the muscle fiber axis. We identified this axis and computationally rotated images to align the fibers vertically and the sarcomere bands horizontally. We multiplied each image column by a Hamming window and computed a discrete Fourier transform of each column image. We band-pass filtered the spatial frequency spectrum to isolate frequencies corresponding to sarcomere periods of 1–5 μm (Llewellyn et al., 2008). To reduce noise in the pass-band, we window-averaged spectra of adjacent columns across the entire image. We used a least-squares fit of a Gaussian profile to locate the peak frequency in the pass-band for each column and recorded the corresponding sarcomere period. We reported the mean sarcomere length for the image as the mean period from all columns.

This analysis relied on identification of sarcomere A-band centers. The A-bands appeared blurred in our images; nevertheless, we could accurately measure the total span of many tens of sarcomeres to within our instrument's resolution limit, since blurring was symmetric about the A-band midlines. After dividing the image span by the number of sarcomeres therein, the SEM of the mean sarcomere length determination was a fraction of the resolution limit. In practice, we made the determinations in the Fourier domain, but the SEM values were tens of nanometers for analogous reasons. To verify the precision of our procedures, we computed the SD of mean sarcomere lengths determined from several series of successive, identically acquired images. This revealed that the SD of the mean sarcomere length determined from the different individual images in a given series was ~30 nm.

In animal and human imaging studies we found substantial heterogeneity in sarcomere lengths between the individual fibers of a muscle. In some cases, even adjacent fibers had mean sarcomere lengths that differed by up to 10%. The s.d. between sarcomere lengths in neighboring fibers was typically 0.1–0.3 μm, an order of magnitude larger than the measurement precision of our microscope. We verified that this heterogeneity was characteristic of skeletal muscle, and was not introduced by measurement errors or due to optical signals originating slightly outside the focal plane, by imaging excised rodent skeletal muscle under a commercial two-photon microscope and observing the same phenomenon. To improve estimates of the global mean sarcomere length in a muscle, we typically measured and averaged sarcomere lengths in 10 separate fibers at a single injection site, by gradually raising the microscope via its translation stage and thus withdrawing the microendoscope by small distances. This approach usually reduced the SEM across the 10 fibers to 0.03–0.1 μm.

We also observed that insertion of the microendoscope caused a slight but consistent stretch in the fibers as they deformed around the needle, slightly lengthening the measured mean sarcomere length. To correct for this lengthening we empirically assessed its magnitude. We inserted our probes into rodent muscle and fixed the muscle with the needle in place. We then sectioned the tissue orthogonal to the needle axis to image how the fiber trajectories deformed around the puncture site. We used a commercial two-photon microscope to image sarcomeres close to the needle surface that would be observed by the microendoscope probe, and we compared the sarcomere lengths to those several millimeters away, where the deformation was absent. This showed that the probe yields mean sarcomere lengths 11% ± 2% (mean ± SEM.) greater than those distal to the injection site. Thus, we reduced all measured sarcomere lengths by this 11% factor. Since the noise in this factor was less than the inherent heterogeneity in sarcomere lengths across the different fibers of a muscle, the latter was the dominant source of variability in our measurement process.

Analysis of Contractile Speeds

To examine contracting sarcomeres in line-scan images taken during electrical stimulation, we used a peak-finding algorithm to identify corresponding sarcomere bands between successive lines and compute their mean displacement. We repeated this procedure for the duration of the line scan and made plots of sarcomere displacement versus time, from which we measured contraction and half-relaxation times. We calculated the mean sarcomere length for each line analogously to how we determined the mean sarcomere length in relaxed muscle. However, to preserve temporal resolution, we reduced the number of neighboring lines in each spectral window average.

Analysis of Sarcomere and Tendon Force Dynamics

We anesthetized mice with isoflurane (1%–3%) and kept them warm on a heating pad. We shaved the hind limb, exposed the sciatic nerve and the triceps surae muscle group of the lower limb, isolated the Achilles tendon, and cut the calcaneus. We attached a force transducer (0.3 mN resolution, Aurora Scientific, 300C-LR) to the calcaneus bone piece at the tendon via a lightweight, rigid hook. We positioned the wearable microscope next to the exposed muscle and punctured the belly of the medial gastrocnemius with the microendoscope.

To initiate motor neuron activity, we stimulated contractions via the microendoscope probe while imaging the sarcomeres. The transducer reported the muscle's contractile dynamics, which we recorded at 10 kHz and converted from analog to digital (PCI-6251, National Instruments). We determined passive muscle tension using the data from each trial prior to electrical stimulation. The force traces of Figure 4 show the total force as a function of time, minus the passive force. To determine the supra-maximal twitch force, we placed a custom-built stimulation cuff around the sciatic nerve and applied electrical stimulation (S48 Stimulator, Grass Technologies). We determined a supra-maximal stimulation level for each mouse by increasing the voltage until the twitch force amplitudes reached a plateau.

Abolishment of Twitches upon Blockade of Neuromuscular Transmission

We anesthetized mice and inserted the microendoscope into the gastrocnemius in the same manner as for tendon force measurements, but without cutting the calcaneus. We elicited 1 Hz twitch contractions by electrical stimulation via the microendoscope while concurrently imaging the sarcomeres. After 1 min of consistent contractions, we injected the nicotinic acetylcholine receptor antagonist atracurium besylate (5 mg/kg, Santa Cruz Biotechnology) intrapertioneally. We recorded the gradual disappearance of the evoked contractions starting at 10 min post-injection.

Statistical Analysis

We performed all analyses in MATLAB (MathWorks) (RRID: nlx_153890). We used a two-tailed Wilcoxon rank sum test to assess the statistical significance of differences in contractile speeds and sarcomere lengths between groups.

SUPPLEMENTAL INFORMATION

Supplemental Information includes three figures and can be found with this article online at http://dx.doi.org/10.1016/j.neuron.2015.11.022.

AUTHOR CONTRIBUTIONS

G.N.S., S.L.D., and M.J.S. conceived the project, designed experiments, and wrote the paper. G.N.S. designed and built the microscope. G.N.S. and S.S. characterized the optical performance. G.N.S. and H.L. performed experiments in mice. G.N.S. and X.C. performed experiments in humans. V.N. oversaw and recruited post-stroke patients. S.L.D. and M.J.S. supervised the work.

ACKNOWLEDGMENTS

We thank L.D. Burns, E.D. Cocker, M.J. Cromie, E.T.W. Ho, J. Jaramillo, J.C. Jung, J. Kiratli, K. McGill, J. Savall, and A. Silder for helpful conversations and technical assistance. We appreciate funding from the Stanford Bio-X Program (S.L.D., M.J.S.), the Coulter Foundation (S.L.D., M.J.S.), a Stanford Graduate Fellowship (G.N.S.), an NIH Biotechnology training grant (G.N.S), and an NSF Fellowship (X.C.). To disseminate the imaging technology described here, G.N.S., S.L.D., and M.J.S. have co-founded Zebra Medical Technologies Inc. and have a financial interest in the company.

Received: June 24, 2015
Revised: October 28, 2015
Accepted: November 10, 2015
Published: December 16, 2015

REFERENCES

Adrian, E.D., and Bronk, D.W. (1929). The discharge of impulses in motor nerve fibres: Part II. The frequency of discharge in reflex and voluntary contractions. J. Physiol. *67*, i3–i151.

Arnold, E.M., Ward, S.R., Lieber, R.L., and Delp, S.L. (2010). A model of the lower limb for analysis of human movement. Ann. Biomed. Eng. *38*, 269–279.

Barretto, R.P., Messerschmidt, B., and Schnitzer, M.J. (2009). In vivo fluorescence imaging with high-resolution microlenses. Nat. Methods *6*, 511–512.

Bichler, E., and Celichowski, J. (2001). Mechanomyographic signals generated during unfused tetani of single motor units in the rat medial gastrocnemius muscle. Eur. J. Appl. Physiol. *85*, 513–520.

Bowman, W.C. (2006). Neuromuscular block. Br. J. Pharmacol. *147* (*Suppl 1*), S277–S286.

Burke, R.E., Levine, D.N., and Zajac, F.E., 3rd (1971). Mammalian motor units: physiological-histochemical correlation in three types in cat gastrocnemius. Science *174*, 709–712.

Campagnola, P. (2011). Second harmonic generation imaging microscopy: applications to diseases diagnostics. Anal. Chem. *83*, 3224–3231.

Chen, X., Nadiarynkh, O., Plotnikov, S., and Campagnola, P.J. (2012). Second harmonic generation microscopy for quantitative analysis of collagen fibrillar structure. Nat. Protoc. *7*, 654–669.

Ciciliot, S., Rossi, A.C., Dyar, K.A., Blaauw, B., and Schiaffino, S. (2013). Muscle type and fiber type specificity in muscle wasting. Int. J. Biochem. Cell Biol. *45*, 2191–2199.

Cromie, M.J., Sanchez, G.N., Schnitzer, M.J., and Delp, S.L. (2013). Sarcomere lengths in human extensor carpi radialis brevis measured by microendoscopy. Muscle Nerve *48*, 286–292.

Cutts, A. (1988). The range of sarcomere lengths in the muscles of the human lower limb. J. Anat. *160*, 79–88.

D'Antona, G., Pellegrino, M.A., Adami, R., Rossi, R., Carlizzi, C.N., Canepari, M., Saltin, B., and Bottinelli, R. (2003). The effect of ageing and immobilization on structure and function of human skeletal muscle fibres. J. Physiol. *552*, 499–511.

Delp, S.L., Statler, K., and Carroll, N.C. (1995). Preserving plantar flexion strength after surgical treatment for contracture of the triceps surae: a computer simulation study. J. Orthop. Res. *13*, 96–104.

Drey, M., Grösch, C., Neuwirth, C., Bauer, J.M., and Sieber, C.C. (2013). The Motor Unit Number Index (MUNIX) in sarcopenic patients. Exp. Gerontol. *48*, 381–384.

Drey, M., Krieger, B., Sieber, C.C., Bauer, J.M., Hettwer, S., and Bertsch, T.; DISARCO Study Group (2014). Motoneuron loss is associated with sarcopenia. J. Am. Med. Dir. Assoc. *15*, 435–439.

Eberstein, A., and Goodgold, J. (1968). Slow and fast twitch fibers in human skeletal muscle. Am. J. Physiol. *215*, 535–541.

Edgerton, V.R., Smith, J.L., and Simpson, D.R. (1975). Muscle fibre type populations of human leg muscles. Histochem. J. *7*, 259–266.

Edman, K.A. (1979). The velocity of unloaded shortening and its relation to sarcomere length and isometric force in vertebrate muscle fibres. J. Physiol. *291*, 143–159.

Flusberg, B.A., Cocker, E.D., Piyawattanametha, W., Jung, J.C., Cheung, E.L., and Schnitzer, M.J. (2005). Fiber-optic fluorescence imaging. Nat. Methods *2*, 941–950.

Friedrich, O., Both, M., Weber, C., Schürmann, S., Teichmann, M.D., von Wegner, F., Fink, R.H., Vogel, M., Chamberlain, J.S., and Garbe, C. (2010). Microarchitecture is severely compromised but motor protein function is preserved in dystrophic mdx skeletal muscle. Biophys. J. *98*, 606–616.

Galea, V., Fehlings, D., Kirsch, S., and McComas, A. (2001). Depletion and sizes of motor units in spinal muscular atrophy. Muscle Nerve *24*, 1168–1172.

Garnett, R.A., O'Donovan, M.J., Stephens, J.A., and Taylor, A. (1979). Motor unit organization of human medial gastrocnemius. J. Physiol. *287*, 33–43.

Gollapudi, S.K., and Lin, D.C. (2009). Experimental determination of sarcomere force-length relationship in type-I human skeletal muscle fibers. J. Biomech. *42*, 2011–2016.

Gollnick, P.D., Sjödin, B., Karlsson, J., Jansson, E., and Saltin, B. (1974). Human soleus muscle: a comparison of fiber composition and enzyme activities with other leg muscles. Pflugers Arch. *348*, 247–255.

Gordon, A.M., Huxley, A.F., and Julian, F.J. (1966). The variation in isometric tension with sarcomere length in vertebrate muscle fibres. J. Physiol. *184*, 170–192.

Griffiths, R.I. (1991). Shortening of muscle fibres during stretch of the active cat medial gastrocnemius muscle: the role of tendon compliance. J. Physiol. *436*, 219–236.

Hartree, W., and Hill, A.V. (1921). The nature of the isometric twitch. J. Physiol. *55*, 389–411.

Henneman, E. (1957). Relation between size of neurons and their susceptibility to discharge. Science *126*, 1345–1347.

Hicks, J.L., Delp, S.L., and Schwartz, M.H. (2011). Can biomechanical variables predict improvement in crouch gait? Gait Posture *34*, 197–201.

Hultman, E., Sjöholm, H., Jäderholm-Ek, I., and Krynicki, J. (1983). Evaluation of methods for electrical stimulation of human skeletal muscle in situ. Pflugers Arch. *398*, 139–141.

Liddell, E.G.T., and Sherrington, C.S. (1925). Recruitment and some other factors of reflex inhibition. Proc. R. Soc. Lond. B Biol. Sci. *97*, 488–518.

Llewellyn, M.E., Barretto, R.P., Delp, S.L., and Schnitzer, M.J. (2008). Minimally invasive high-speed imaging of sarcomere contractile dynamics in mice and humans. Nature *454*, 784–788.

Logigian, E.L., Twydell, P., Dilek, N., Martens, W.B., Quinn, C., Wiegner, A.W., Heatwole, C.R., Thornton, C.A., and Moxley, R.T., 3rd (2010). Evoked myotonia can be "dialed-up" by increasing stimulus train length in myotonic dystrophy type 1. Muscle Nerve *41*, 191–196.

Manole, A., Fratta, P., and Houlden, H. (2014). Recent advances in bulbar syndromes: genetic causes and disease mechanisms. Curr. Opin. Neurol. *27*, 506–514.

Muir, R.B., and Lemon, R.N. (1983). Antidromic excitation of motoneurons by intramuscular electrical stimulation. J. Neurosci. Methods *8*, 73–86.

Nandedkar, S.D., Barkhaus, P.E., and Stålberg, E.V. (2010). Motor unit number index (MUNIX): principle, method, and findings in healthy subjects and in patients with motor neuron disease. Muscle Nerve *42*, 798–807.

Nelson, D.L., Orr, H.T., and Warren, S.T. (2013). The unstable repeats–three evolving faces of neurological disease. Neuron *77*, 825–843.

Plotnikov, S.V., Millard, A.C., Campagnola, P.J., and Mohler, W.A. (2006). Characterization of the myosin-based source for second-harmonic generation from muscle sarcomeres. Biophys. J. *90*, 693–703.

Plotnikov, S.V., Kenny, A.M., Walsh, S.J., Zubrowski, B., Joseph, C., Scranton, V.L., Kuchel, G.A., Dauser, D., Xu, M., Pilbeam, C.C., et al. (2008). Measurement of muscle disease by quantitative second-harmonic generation imaging. J. Biomed. Opt. *13*, 044018.

Pontén, E., Gantelius, S., and Lieber, R.L. (2007). Intraoperative muscle measurements reveal a relationship between contracture formation and muscle remodeling. Muscle Nerve *36*, 47–54.

Ralston, E., Swaim, B., Czapiga, M., Hwu, W.L., Chien, Y.H., Pittis, M.G., Bembi, B., Schwartz, O., Plotz, P., and Raben, N. (2008). Detection and imaging of non-contractile inclusions and sarcomeric anomalies in skeletal muscle by second harmonic generation combined with two-photon excited fluorescence. J. Struct. Biol. *162*, 500–508.

Rose, J., Haskell, W.L., Gamble, J.G., Hamilton, R.L., Brown, D.A., and Rinsky, L. (1994). Muscle pathology and clinical measures of disability in children with cerebral palsy. J. Orthop. Res. *12*, 758–768.

Sammarco, G.J., Bagwe, M.R., Sammarco, V.J., and Magur, E.G. (2006). The effects of unilateral gastrocsoleus recession. Foot Ankle Int. *27*, 508–511.

Saporta, A.S., Sottile, S.L., Miller, L.J., Feely, S.M., Siskind, C.E., and Shy, M.E. (2011). Charcot-Marie-Tooth disease subtypes and genetic testing strategies. Ann. Neurol. *69*, 22–33.

Serra, A., Ruff, R., Kaminski, H., and Leigh, R.J. (2011). Factors contributing to failure of neuromuscular transmission in myasthenia gravis and the special case of the extraocular muscles. Ann. N Y Acad. Sci. *1233*, 26–33.

Shefner, J.M., Watson, M.L., Simionescu, L., Caress, J.B., Burns, T.M., Maragakis, N.J., Benatar, M., David, W.S., Sharma, K.R., and Rutkove, S.B. (2011). Multipoint incremental motor unit number estimation as an outcome measure in ALS. Neurology *77*, 235–241.

Sica, R.E., and McComas, A.J. (1971). Fast and slow twitch units in a human muscle. J. Neurol. Neurosurg. Psychiatry *34*, 113–120.

Smith, L.R., Lee, K.S., Ward, S.R., Chambers, H.G., and Lieber, R.L. (2011). Hamstring contractures in children with spastic cerebral palsy result from a stiffer extracellular matrix and increased in vivo sarcomere length. J. Physiol. *589*, 2625–2639.

Sreedharan, J., and Brown, R.H., Jr. (2013). Amyotrophic lateral sclerosis: Problems and prospects. Ann. Neurol. *74*, 309–316.

Taylor, A., and Stephens, J.A. (1976). Study of human motor unit contractions by controlled intramuscular microstimulation. Brain Res. *117*, 331–335.

Vandervoort, A.A., and McComas, A.J. (1986). Contractile changes in opposing muscles of the human ankle joint with aging. J. Appl. Physiol. *61*, 361–367.

Ward, S.R., Eng, C.M., Smallwood, L.H., and Lieber, R.L. (2009). Are current measurements of lower extremity muscle architecture accurate? Clin. Orthop. Relat. Res. *467*, 1074–1082.